



# Enhanced electron density and plasma dynamics on nanosecond time scales in Helium plasma discharges

H. Y. Kim<sup>a</sup> , M. Gołkowski, and V. Harid

Department of Electrical Engineering, University of Colorado Denver, Denver, CO 80204, USA

Received 1 December 2020 / Accepted 1 April 2021 / Published online 19 April 2021  
© The Author(s), under exclusive licence to EDP Sciences, SIF and Springer-Verlag GmbH Germany, part of Springer Nature 2021

**Abstract.** Enhanced electron density and plasma dynamics are investigated for Helium discharges on nanosecond timescales with Particle-In-Cell simulations. The plasma discharges are driven between planar electrodes with DC, single pulses, and dynamic frequency square waves. It is assumed that the DC and pulse discharges operate in the glow regime. It is shown that as pressure increases with narrowing gap distance, the peak transient electron density rises. This is in contrast to what is observed under a constant pressure-gap ( $pd$ ) and electric field reduced by neutral density ( $E/N$ ) values at saturation time. It is shown that although the  $pd$  and  $E/N$  values and therefore the breakdown voltage are the same across cases, the plasma kinetics are different due to a change in the energy relaxation lengths. The cross-points between the sheath length and energy relaxation length move to higher electron energies at higher pressure. This facilitates high-energy electrons to undergo inelastic collisions and produces different rates of increasing electron density and temperature at nanosecond timescales. Moreover, using a plasma frequency-dependent square wave, the electron density can be increased to 50 times higher over that of the DC case because of a reverse electric field. The electron kinetics on nanosecond time scales can be exploited for high electron density and fast ionization applications.

## 1 Introduction

Plasma discharges on nanosecond time scales are crucial for many applications including dynamic plasma antennas, plasma chemical fuel reforming, high-speed flow control, plasma channels, and generation of high-energy electrons [1–6]. Moreover, such discharges can enable the delivery of highly reactive plasma species in a non-destructive way and can be used to selectively heat sensitive surfaces. Plasma-surface interactions are important for the fabrication of microprocessors and can also be leveraged in liquids, organic tissues and wounds, as part of the emerging field of plasma medicine [7–10]. The original motivation behind this work was to achieve the fastest possible increase in electron density for dynamic plasma antennas, in which the conducting properties of a plasma column are changed on the order of the propagation time of a radiating surface wave [11–13]. For the dynamic plasma antenna, Cohen et al. [11–13] recently investigated plasma dynamics for a variety of pressures, gap distances between electrodes, and ionizing voltages on nanosecond time scale with optical measurements.

To identify optimal plasma conditions for rapid ionization and high electron density on nanosecond scales,

we investigate plasma dynamics using similarity laws that have played an important role in describing the electron kinetics [14]. The similarity laws have been analyzed in terms of gas pressure, electrode geometry, power source, discharge condition, formation time, etc. [14–17]. Among these parameters, the pressure-gap ( $pd$ ) product and electric field reduced by neutral density ( $E/N$ ) were widely used for parameterizing gas ionization between two electrodes [18–22]. At  $pd$  values below 0.4 Torr cm, breakdown voltages are quite different even if the  $pd$  values are the same with different gap between the electrodes [20, 21]. However, at relatively high  $pd$  values ( $> 1$  Torr cm), the similarity relations have been shown to have a linear dependence with gas temperature ( $T$ ) and shifts can be explained based on the ideal gas law [22]. For various gas temperatures, alternative  $pd/T$  scaling has been employed to achieve better agreement with experimental results [22]. Current density ( $J$ ) reduced by pressure ( $J/p^2$ ) scaling at fixed  $pd$  values was investigated with a realistic diameter of the discharges by Petrović et al. [20]. Overall, there have been numerous investigations of the accuracy of the similarity laws at variable values of pressure, gap distance, and gas type on the order of microseconds and nanoseconds [18, 23–26].

For applications where a dense plasma ( $10^{18}$ – $10^{20}$  m<sup>-3</sup>) is desired, researchers have studied initial electron avalanches like runaway electrons [27–29]. These

<sup>a</sup> e-mail: [hoyoung.kim@ucdenver.edu](mailto:hoyoung.kim@ucdenver.edu) (corresponding author)

**Table 1** Simulation condition for operating pressures and gap distance between two electrodes with applied voltage and secondary emission electron coefficients;  $p$  = pressure (Torr),  $d$  = gap distance (cm),  $E$  = electric field (V/cm), and  $N$  = neutral density

	$p$ (Torr)	$d$ (cm)	$pd$ (Torr cm)	$E/N$ (Td)
Case 1	1	10	10	190
Case 2	10	1	10	190
Case 3	100	0.1	10	190

runaway electrons ( $> 1$  keV) have been investigated for their acceleration by an electric field along a mean free path with few inelastic collisions [27, 30–34]. However, on the nanosecond time scale in the absence of critical avalanche of runaway electrons in low density plasmas ( $< 10^{18} \text{ m}^{-3}$ ), the variability of the electron kinetics at a constant  $pd$  and  $E/N$  values are still not well-understood. As discussed below, electrons in our simulations have energies less than 100 eV and therefore are not in the regime of critical avalanche.

In this work, we use a fully kinetic model to investigate the same  $pd$  and  $E/N$  values shown in Table 1. It is known that non-equilibrium plasmas may have highly local conditions that make it difficult to quantify behavior with scaling laws using average  $pd$  and  $E/N$  values. Sheath regions and short timescales are conditions under which incomplete relaxation can affect scaling but as plasma density increases macroscopic swarm behavior once again dominates as the plasma is able to enforce quasineutrality [35, 36]. We investigate electron kinetics for DC, single square pulses (SP), and also a special waveform known as a plasma frequency-dependent square wave (PSW). The PSW is a square wave with increasing frequency as described in Ref. [3]. Specifically, it is the sum of single square pulses with progressively shortening durations. Chang et al. [37] explored the electron kinetics in DC argon microplasmas with the same  $pd$  values. A fixed  $pd$  and  $E/N$  values make the number of electron-neutral (e-n) collisions almost the same, which allows direct comparison across different plasmas [37]. The energy relaxation length and mean free path were calculated using cross sections of elastic, excitation, and ionization. At high pressure with a microgap between planar electrodes, electron density was found to be lower compared to low pressure with a large gap. In addition, there are more low energy electrons at the saturation time. However, for nanosecond timescales considered in this work, we suggest that high pressure in nanosecond discharges has fast growing electron densities with different times of potential saturation for sheath extension and different lengths.

## 2 Description of models

Helium (He) gas at constant  $pd$  and  $E/N$  values is modeled by varying the operating pressure and the distance

between two electrodes. We employ a one-dimensional (1d3v) Particle-In-Cell (PIC) simulation (XPDP1 [38–43] with Monte Carlo collisions (MCC), which is self-consistent and fully kinetic. The background neutral He gas is assumed to be uniform between the electrodes. The secondary electron (SE) emission coefficient for He ions is assumed to be 0.1, whereas electrons are assumed to be perfectly absorbed at electrodes [41, 42]. Electrons can undergo elastic, excitation, and ionization collisions. Ions can undergo charge exchange and scattering collisions. The cross sections of the collisions are dependent on electron and ion energies. The MCC uses a null collision method with energy-dependent cross section [43, 44]. The time step is  $1 \times 10^{-13}$  s and the cell size is  $5 \times 10^{-6}$  m which is shorter than the Debye length ( $5.254 \times 10^{-6}$  m). The superparticles are weighted at  $5 \times 10^6$  and the initial number of traced superparticles is  $2 \times 10^6$ . The numbers of superparticles in a cell and in Debye length are 1000 and 1050 [45, 46]. The numbers are the same for all cases. Table 1 shows the simulation conditions for operating pressures, gap distance between electrodes, and electric field reduced by neutral density. Three cases are considered where the  $pd$  and  $E/N$  values are constant at 10 Torr cm and 190 Td. The amplitudes of DC, SP, and PSW cases are 605 V and the voltage is applied at the anode which is the left electrode ( $x = 0$ ) and the grounded cathode is the right electrode. The gas temperatures are fixed at 300 K. The initial electron temperature is set to 0.001 eV for the seed population of  $10^{15} \text{ m}^{-3}$  [3, 4, 10]. The densities of neutral He molecules are dependent on the pressure for each case. The particle Courant–Friedrichs–Lewy (CFL) condition  $\nu \Delta t / \Delta x < 1$ , where  $\nu$  is the particle velocity, is satisfied for all particles [45].

## 3 Results

### 3.1 DC discharges

Figure 1a shows the transient response until 10 ns of average electron density for the three cases of He plasma at the same  $pd$  and  $E/N$  values. The densities are averaged along gap distance for all electrons. For Case 1 (1 Torr), the electron density increases continually ( $1.32 \times 10^{15} \text{ m}^{-3}$  above the seed density). In Case 2 (10 Torr), the electron density initially grows faster than Case 1 but saturates at 4 ns. In Case 3 (100 Torr), the electron density reaches a peak value at 0.82 ns and slightly decreases before 3 ns and is sustained. The reason for this is electrons generated near the anode move out and are absorbed at the electrode as shown in Fig. 4c. Figure 1b shows the transient response of an average electron temperature along gap distance for all electrons for the three cases. In Cases 2 and 3, the electron temperatures each reach a peak value and then decrease. The initial seed electrons are heated by the applied external field and the average electron temperatures increase at different rates. Energetic electrons with energies higher than the threshold energy for ion-

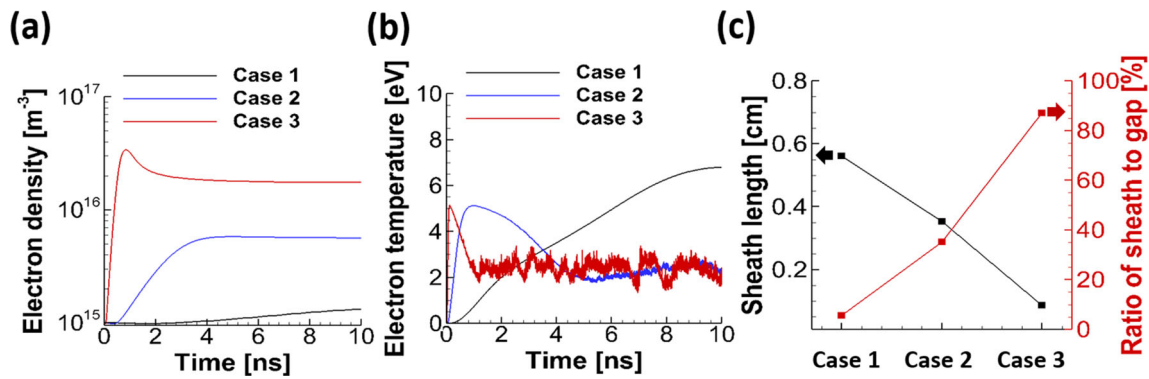


**Fig. 1** PIC simulation results in He DC plasma for 3 cases. **a** Average electron density, **b** Average electron temperature on nanosecond time scale. **c** Sheath length and ratio of sheath length to gap distance at 10 ns in three cases

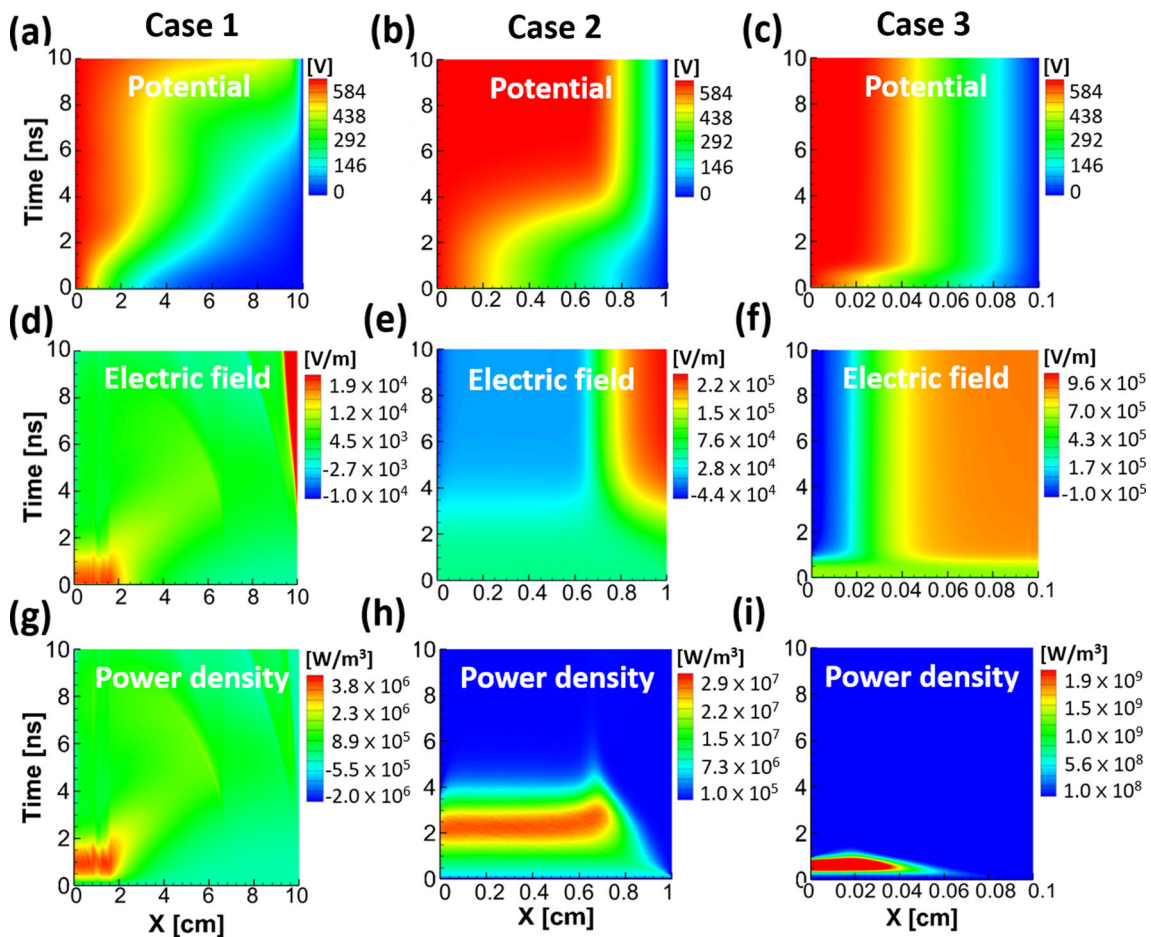


**Fig. 2** Time and space evolution of the potential, electric field, and electron-dissipated power density in He plasma for 605 V DC for Case 1 in panels **a, d, g**, Case 2 in panels **b, e, h**, Case 3 in panels **c, f, i**

ization ( $> 24.5$  eV) drive ionization. Electron densities increase as the electron kinetic energy is transferred to ionization. After reaching a peak temperature, the electron temperature decreases and is sustained. Figure 1c shows the sheath length and ratio of sheath length to gap distance for three cases at 10 ns. The sheath length is defined as the position where the instantaneous ratio of electron density to ion density is 0.5 [3]. When the

pressure increases, the sheath lengths are shorter. However, the ratio of sheath length to gap distance increases with higher pressure. This is in agreement with results shown in Ref. [37]. If electrons gain energies over a longer length then the electrons undergo inelastic collisions which leads to a high electron density. Besides elucidating the breakdown voltage in the similarity laws, these kinetics are relevant for understanding fast dis-

charges with the same  $pd$  value. For example, at a constant  $pd$  value, the electron density, at the saturated time, was shown to decrease as the pressure increases [37]. However, on transient time scales, electron densities increase at high pressure. Case 3 has the highest electron density with a high ratio of sheath to gap distance. This suggests that there is an optimal condition for high and fast growing electron density under constant driven voltage.

Figure 2 shows the time and space evolution of the potential, electric field, and electron dissipated power densities for He 605V DC plasmas for Case 1 in panels (a), (d), (g), Case 2 in panels (b), (e), (h), and Case 3 in panels (c), (f), (i). Figure 2a–c show the transient potential of the three cases. In Case 1, the potential sheath is first saturated at 4 ns and a second sheath is saturated after 10 ns. As shown in Fig. 1b, the electron temperature continually increases until 10 ns. The area of high electric field is the same as the area of high electron-dissipated power density as shown in Fig. 2d, g. With the DC applied voltage, electrons move from cathode to anode and get heated. The movements result in a bulk plasma region and the electron density increases. However, before 10 ns, the steady bulk region is not yet formed as shown in Fig. 2a. In Case 2, the potential is saturated after 4 ns and the electric field is high at the sheath region shown in Fig. 2b, e. For times less than 4 ns, the electron-dissipated power density is high when the bulk region has not yet formed as shown in Fig. 2h. Although the electric field is high in the sheath region after 4 ns, the power density is lower because of low electron density. In Case 3, the potential is saturated at 1 ns and the cathode sheath length is longer than half of the gap distance. After 1 ns, a bulk region is formed and the average electron temperature is sustained as shown in Fig. 1b.

These differences in electron density and time of bulk region formation even at the same  $pd$  and  $E/N$  value can be explained by the different energy relaxation lengths ( $\lambda_\epsilon$ ) as shown in Fig. 3a. Solid lines are the energy relaxation lengths and dotted lines are sheath lengths for the three cases. The energy relaxation lengths in equation (1) below [37, 47, 48] are calculated by the mean free path for elastic collisions ( $\lambda_m$ ) in equation (2) [49] and inelastic collisions ( $\lambda_{inelastic}$ ) in equation (3) where  $n_g$ ,  $\sigma$ ,  $m_e$ ,  $M_{He}$  are, respectively, neutral gas density, cross sections, electron mass, and helium mass [48].

$$\lambda_\epsilon = \sqrt{\frac{\lambda_m \lambda_{inelastic}}{3}} \tag{1}$$

$$\lambda_m = \frac{1}{n_g(\text{Torr})\sigma(\text{eV})} \tag{2}$$

$$\lambda_{inelastic} = \frac{1}{n_g(\text{Torr}) \left( \frac{2m_e}{M_{He}} * \sigma_{ela}(\text{eV}) + \sigma_{ex}(\text{eV}) + \sigma_{ion}(\text{eV}) \right)} \tag{3}$$

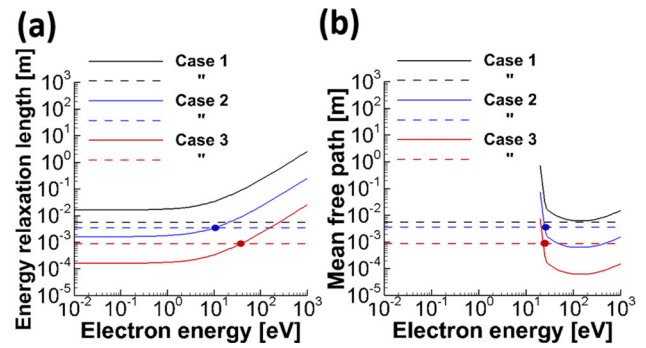
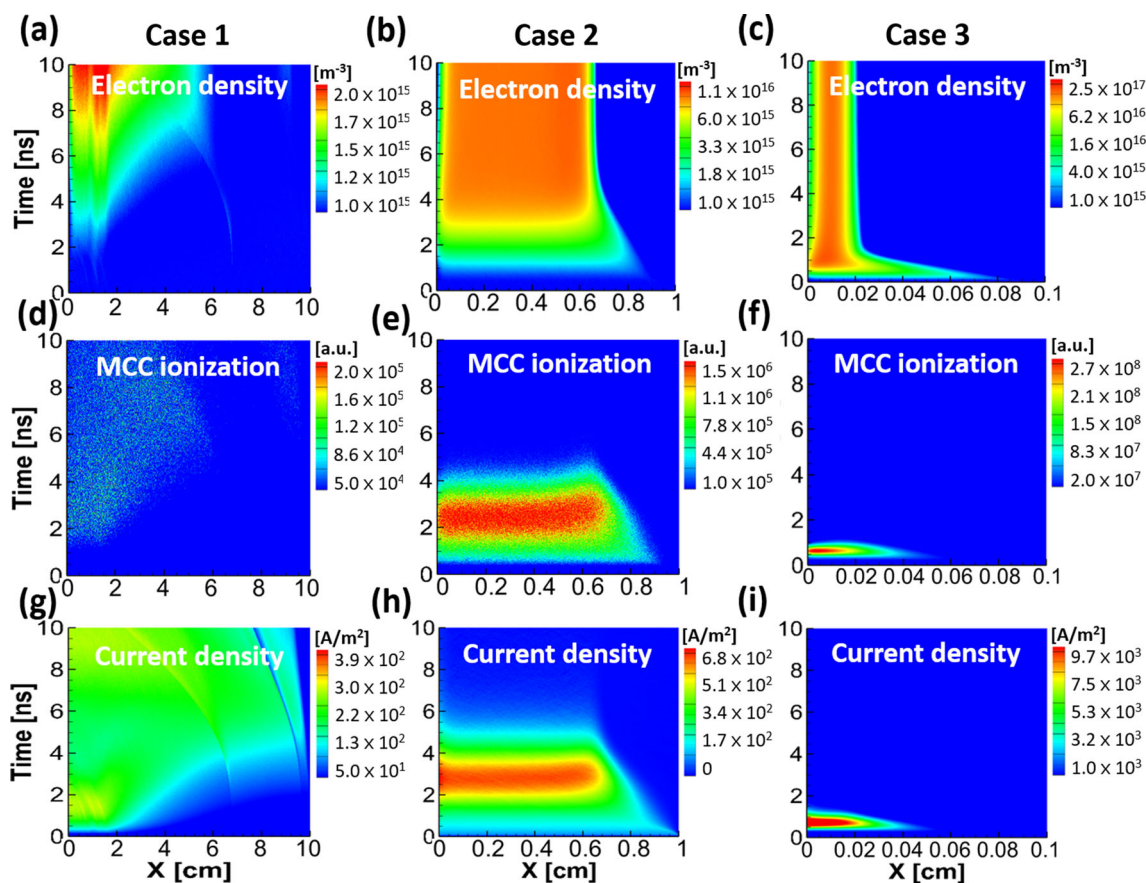


Fig. 3 a Energy relaxation length and b mean free path with electron energy at 10 ns. Dotted lines are sheath length for three cases

The cross sections are dependent on electron energy for elastic, excitation, and ionization collisions [43, 44]. The energy relaxation length represents the minimum length for energy loss by collisions. For example, electrons that have less energy than the energies at the cross-point between sheath length and energy relaxation length can undergo collisions resulting in energy loss. At high pressure, the cross-points between the sheath and energy relaxation length are demarked with dots that move toward higher electron energy with an increase in pressure. This implies that more high-energy electrons can undergo excitation and ionization collisions because the cross-point is higher than the threshold energies for excitations and ionizations. This explains why there are different saturation times for sheath extension and electron densities. Figure 3b shows mean free paths (solid) for ionization and sheath lengths (dotted) with electron energy for three cases. In Case 1, the sheath region is not formed, and there is no cross-point between the mean free path and sheath length until 10 ns. In Cases 2 and 3, the cross-points are at the same energy because the  $pd$  value is the same.

Figure 4 shows time and space evolution of electron density, MCC ionization, and current density for Case 1 in panels (a), (d), (g), Case 2 in panels (b), (e), (h), and Case 3 in panels (c), (f), (i). Figure 4a–c show the transient responses of the electron densities. In Case 1, initial electrons move from the cathode to the anode as shown in Fig. 4g. The electron density nearby the anode sheath increases as shown in Fig. 4a. The number where MCC ionizations occur is higher in bulk and anode sheath regions as shown in Fig. 4d. With MCC ionizations, electron density increases and the bulk region is formed as shown in Fig. 4a. In Case 2, Fig. 4b shows the profile of electron density is typical for DC plasma discharges [50]. The anode sheath is shorter than the cathode and electron density is higher at the bulk toward the cathode. At 0.95 ns, the first electron temperature is 5.12 eV shown in Fig. 1b. After 0.95 ns, electron density increases from the anode sheath and bulk region shown in Fig. 4b. At 2.6 ns, current density and the number of MCC ionizations are the highest at 0.6 cm and decreases as shown in Fig. 4e and h. After 4 ns, ionizations decrease and the transient electron density is not



**Fig. 4** Time and space evolution of the electron density, the number of MCC ionization, and current density for 605 V He DC plasmas for Case 1 in panels a, d, g, Case 2 in panels b, e, h, Case 3 in panels c, f, i

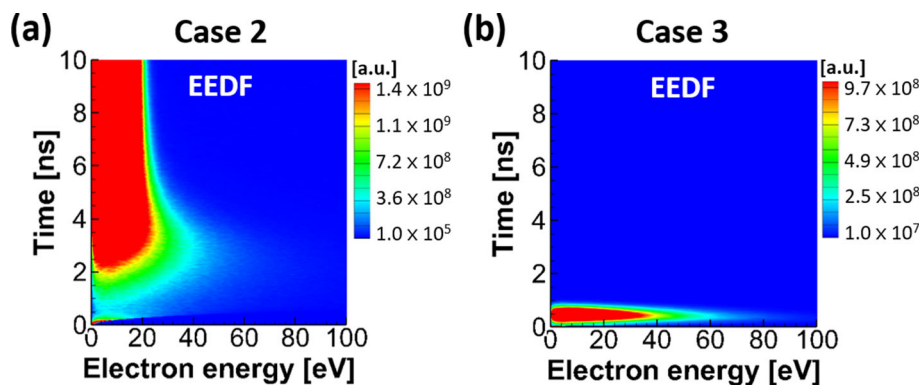


**Fig. 5** Time and particle energy evolution of the electron energy distribution function (EEDF) at the center for Case 2 in panels a, Case 3 in panels b

changed. This is why average electron density is saturated as shown in Fig. 1a. In Case 3, before 0.9 ns, there are highly ionizing collisions in the anode and narrow bulk shown in Fig. 4f. After 0.9 ns, Fig. 4c shows electrons at the anode sheath move out toward the anode and electron density decreases at the anode sheath. The movement leads to a slight decrease in average electron density shown in Fig. 1a. At times less than 4 ns, the electron density is saturated and most of the electrons

are in the bulk region and the anode sheath shown in Fig. 4c.

Figure 5 shows the time and particle energy evolution of the electron energy distribution function (EEDF) at the center for Case 2 and 3. In Case 2, after 1 ns, there are energetic electrons with energies higher than the threshold energy for ionization as shown in Fig. 5a. The electrons undergo ionization collisions as shown in Fig. 4e. In Case 3(a), at 0.8 ns, most electrons have energies less than 40 eV. After 0.8 ns, high-energy elec-

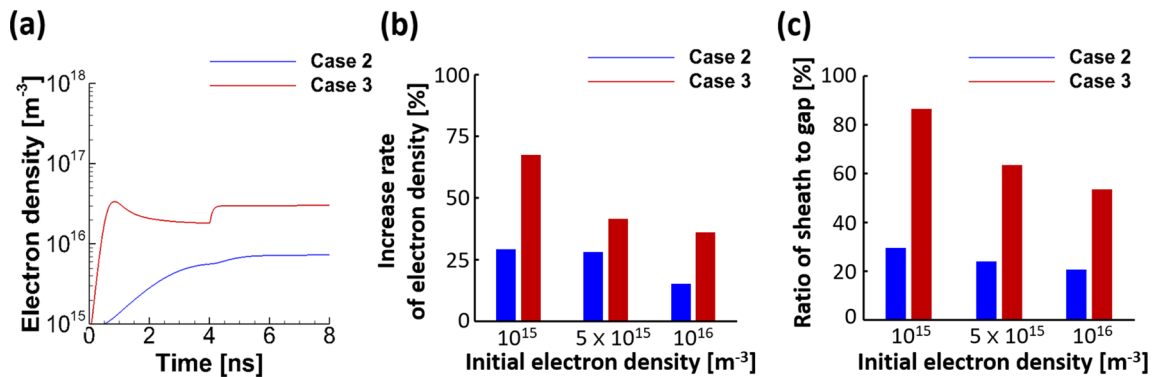


**Fig. 6** a Time evolution of average electron density with 4 ns single square pulse and b increase rate of electron density between at 4 ns and at 8 ns with different initial electron density. c Ratio of sheath to gap for Case 2 and 3 with different initial electron density

trons are reduced and the average electron temperature also decreases as shown in Fig. 1b.

### 3.2 Single pulse (SP) and plasma square wave (PSW)

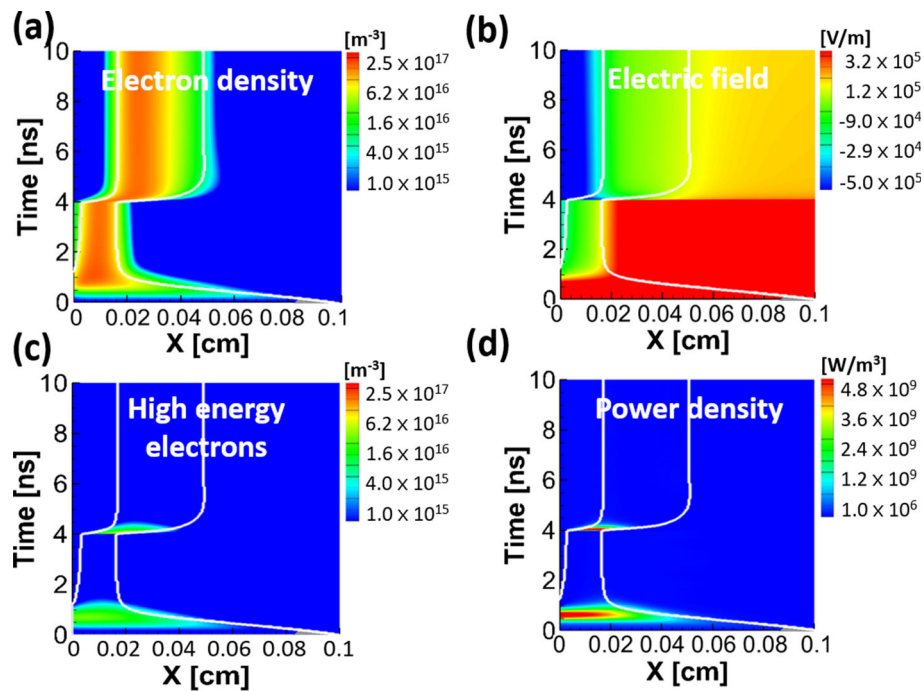
Figure 6a shows the time evolution of average electron density when driven by a 4 ns single pulse (SP) for Case 2 and Case 3. The electron density is averaged along the gap distance between two electrodes with all electron particles. The SP has a trapezoidal shape consisting of rising, sustain, and falling time. The rise and fall time is 42 ps and the voltage is terminated at 4 ns. The rise time with 605 V is based on hardware that was recently developed at Picosecond Pulse Lab, Inc (model 5531). In practice, one must be careful in assuming that the voltage on realistic electrodes will not be degraded by circuit impedances and parasitic reactance. We thus use the hardware specs here as an expected best case. After 4 ns, there are potential drops between the bulk region and the anode since the anode has changed from positive to zero potential. This applied potential leads to reversal of electric field that was shown recently by Kim et al. [4] and earlier by others [31, 51] to automatically occur upon applied field termination. With the reversed electric field, the electron density for Case 2 and Case 3 sharply increases as shown in Fig. 6a. Figure 6b shows the rates of electron density increase which are calculated by the ratio of different electron density between before and after SP termination ( $= (N_e @ 8 \text{ ns} - N_e @ 4 \text{ ns}) / N_e @ 4 \text{ ns}$ ) where  $N_e$  is average electron density. The increase rates are dependent on initial electron density. For Case 2, rates decrease from 29.3 to 15.3% as the initial electron density increases from  $10^{15}$  to  $10^{16} \text{ m}^{-3}$ . For Case 3, increase rates also decrease from 67.4 to 36.2% as the initial electron density increases from  $10^{15}$  to  $10^{16} \text{ m}^{-3}$ . All cases in Case 3 have higher increase rates and specifically the rate is 2.3 times higher than those in Case 2 at  $10^{15}$  initial  $N_e$ . This increase can be explained with the ratio of sheath to gap as shown in Fig. 6c. At  $10^{15}$

initial  $N_e$ , the ratio has 87% of the maximum value for Case 3. The electrons can undergo inelastic collisions with higher energy, which is at the cross-point between sheath length and energy relaxation length as shown in Fig. 3a, than that in other cases. This leads to the electron density for Case 3 increasing 4.19 times higher than that for Case 2 as shown in Fig. 6a.

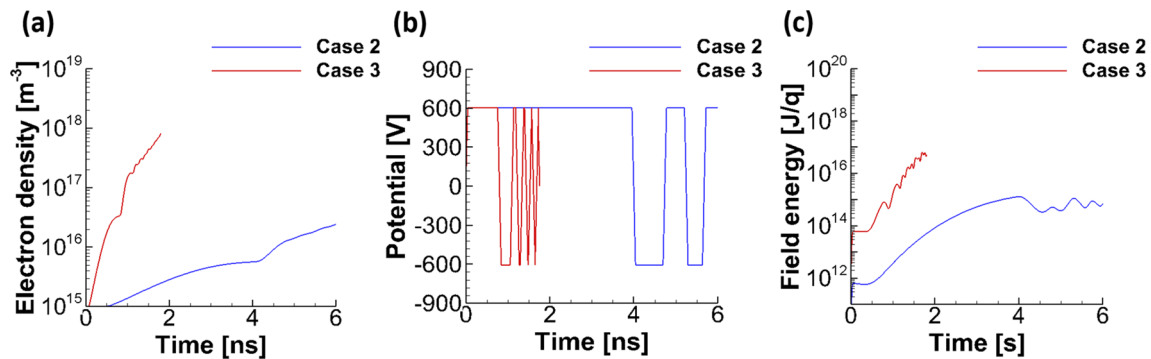
Figure 7 shows the time and space evolution of all electrons, high energy electrons ( $T_e > 24.5 \text{ eV}$ ), electric field, and power density for Case 3. High-energy electrons can undergo ionization collisions. After 4 ns, there is a reverse electric field as shown in Fig. 7b. The reverse field causes the anode sheath and bulk regions to move toward the cathode. Figure 7a shows all electrons move toward the cathode with the reverse field. The electron movement manifests itself as an electron current density with significant electron dissipated power ( $J_e \cdot E$ ) as shown in Fig. 7d. With the reverse electric field, electrons get energies and high energy electrons are generated as shown in Fig. 7c. Most of the electrons are moved from the bulk region toward cathode and the electron density increases. The bulk region is shifted toward cathode and the length is extended from 0.015 to 0.032 cm as shown in Fig. 7a.

Figure 8a shows the transient response of average electron density with a plasma square wave (PSW) for Case 2 and Case 3 of He plasma at the same  $pd$  and  $E/N$  values. A PSW is a square wave with increasing frequency corresponding to the instantaneous plasma frequency as described in Ref. [3]. Specifically, the instantaneous frequency for PSW is half of the instantaneous plasma frequency [3]. For example, in Case 3, at 0.8 ns, the plasma frequency is 1.64 GHz and the polarity of the PSW changes after 0.3 ns which is a half of the plasma period (0.6 ns). In Cases 3 with PSW, the driven voltage polarity is changed at 0.8 ns, when the potential is saturated by the formed bulk region as shown in Fig. 2c. After 0.8 ns, the polarity is changed with the instantaneous plasma frequency.

The average electron density continually increases because of reverse fields as shown in Fig. 8a. The density



**Fig. 7** Time and space evolution of **a** all electrons, **b** electric field, **c** high-energy electrons ( $T_e > 24.5$  eV), and **d** electron-dissipated power density for Case 3. White lines indicate the movement of the sheath edges adjacent to both electrodes. The sheath edge is defined as the position where is instantaneous ratio of electron density to ion density is 0.5 and is updated at every time step



**Fig. 8** PIC simulation results in He with PSW for Case 2 and Case 3. **a** Averaged electron density, **b** waveforms for PSW. **c** Field energy per unit charge

is almost 50 times higher than Case 3 with DC voltage. In Case 2, at 4 ns, the average electron density and the potential are saturated by the formed bulk region as shown in Figs. 1a and 2b. After 4 ns with the change in driven voltage polarity, the average electron density sharply increases as shown in Fig. 8a. The extra ionization is from the release of field energy from the plasma bulk region. The stored energy in the bulk plasma can be calculated from the electric field from plasma charge separation [3]. With the change in driven voltage polarity, field energy decreases and the energy transfers to electron energies for inelastic collisions [3]. The electron density with the change in polarity increase with decreased field energy as shown in Fig. 8a and c.

Figure 9 shows the time and space evolution of all electrons, low energy electrons ( $T_e < 19.8$  eV), high energy electrons ( $T_e > 24.5$  eV), and MCC ionization for Case 3 PSW. After 0.8 ns, electrons get energies with the change in driven voltage polarity because of additional acceleration from the plasma induced reverse electric field [3]. There are high-energy electrons that lead to ionizing collisions in the bulk region as shown in Fig. 9c. Ionization collisions happen from the bulk region to the right electrode as shown in Fig. 9d. After 1.1 ns, with the change in the voltage polarity, electrons are heated and the electron density increases toward the anode as shown in Fig. 9a. After 1.23 ns, the electron density continually increases and the bulk region is 2.6

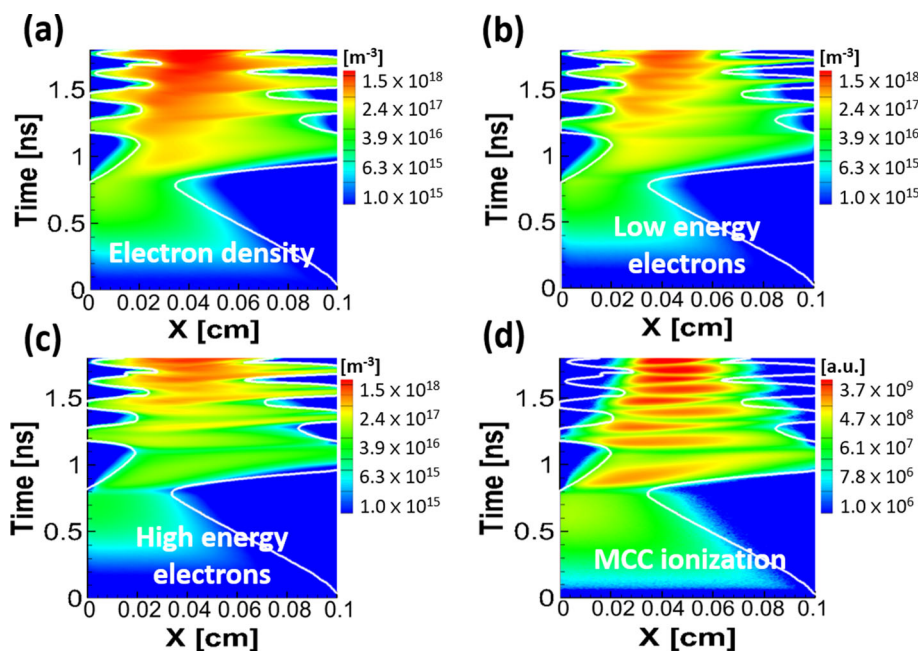


**Fig. 9** In Case 3 PSW, the time and space evolution of **a** all electrons, **b** low-energy electrons ( $T_e < 19.8$  eV), **c** high-energy electrons ( $T_e > 24.5$  eV), and **d** the number of MCC ionization. White lines indicate the movement of the sheath edges adjacent to both electrodes

times extended compared to that at 0.8 ns. The ionization collisions mostly happen in the extended bulk region as shown in Fig. 9d. After ionization collisions, there are more low energy electrons that undergo elastic collisions in the bulk region as shown in Fig. 9b.

## 4 Summary and discussion

Enhanced electron density and plasma dynamics for He plasmas with constant  $pd$  and  $E/N$  values have been investigated at nanosecond timescales in great detail. When the pressure increases from 1 to 100 Torr, the electron density quickly increases and achieves 10 times higher value. At higher pressure, the ratio of sheath length to gap distance is higher which enhances electron heating. In the case of 100 Torr with 0.1 cm gap distance between planar electrodes, the electron density slightly decreases after 0.82 ns because electrons move toward the anode. Even if the  $pd$  value and the breakdown voltage are the same, the plasma kinetics are different due to different energy relaxation lengths in the three cases considered. The cross-points between the sheath length and energy relaxation length move to higher electron energy at high pressure. This means that higher energy electrons can undergo excitation and ionization collisions. This leads to different rates of electron density and temperature increase in the transient regime. At 10 Torr and 100 Torr, the SP and PSW waveform with dynamic frequencies tied to the instantaneous electron density has been used. In particular, at 100 Torr, the

PSW waveform has 50 times higher and faster growing electron density than that in the DC case.

The results presented herein can be used to identify optimal plasma operating conditions for DC, SP, and PSW waveforms to achieve high electron density and fast ionization without high voltage ( $> 1$  kV) on nanosecond time scales [3, 4, 27, 51–53]. This study has focused on He gas at 10 Torr-cm. He gas can be safely driven by a DC pulse train even without the external current-limiting resistance [54]. At the same time, Penning ionization of impurities with excited states of helium is known to be important and can even become the leading ionization pathway [8]. The effects on excited He molecules and photoemission of electrons at electrodes where UV/VUV photon transport is ‘strongly coupled’ to the (charged particle) dynamics of the discharges will be investigated in the future [55].

In different gases, plasma kinetics are expected to have a similar tendency meaning higher electron density and temperature at higher pressure. However, there is a limit to the optimal pressure since for 1,000 Torr and 0.01 cm gap distance, electron density increases rapidly over a very short time at 0.05 ns but later falls below the seed initial electron density because most of electrons are lost at the anode before forming a bulk region. The rise time of the applied voltage and initial electron density for different pressures therefore needs to be considered.

**Data Availability Statement** This manuscript has no associated data or the data will not be deposited. [Authors’



comment: All data generated during this study are contained in this published article.]

## References

- M. B. Cohen, L. Thompson, N. Opalinski, P. Singletary, M. Walker, C. Chan, M. Gólkowski, IEEE AP-S Symposium on Antennas and Propagation and USNC-URSI Radio Science Meeting (2017)
- K. Takashima, I.V. Adamovich, Z. Xiong, M.J. Kushner, S. Starikovskaia, U. Czarnetzki, D. Luggenhölscher, Phys. Plasmas **18**, 083505 (2011)
- H.Y. Kim, M. Gólkowski, Plasma Sources Sci. Technol. **27**, 105015 (2018)
- H.Y. Kim, M. Gólkowski, C. Gólkowski, P. Stoltz, M.B. Cohen, M. Walker, Plasma Sources Sci. Technol. **27**, 055011 (2018)
- S. Abuazoum, S.M. Wiggins, R.C. Issac, G.H. Welsh, G. Vieux, M. Ganciu, D.A. Jaroszynski, Rev. Sci. Instrum. **82**, 063505 (2011)
- ...I. Adamovich, S.D. Baalrud, A. Bogaerts, P.J. Bruggeman, M. Cappelli, V. Colombo, U. Czarnetzki, U. Ebert, J.G. Eden, P. Favia, D.B. Graves, S. Hamaguchi, G. Hieftje, M. Hori, I.D. Kaganovich, U. Kortshagen, M.J. Kushner, N.J. Mason, S. Mazouffre, S.M. Thagard, H.R. Metelmann, A. Mizuno, E. Moreau, A.B. Murphy, B.A. Niemira, G.S. Oehrlein, Z.L. Petrovic, L.C. Pitchford, Y.K. Pu, S. Rauf, O. Sakai, S. Samukawa, S. Starikovskaia, J. Tennyson, K. Terashima, M.M. Turner, M.C.M. Sanden, A. Vardelle, J. Phys. D: Appl. Phys. **50**, 323001 (2017)
- M. Gólkowski, C. Gólkowski, J. Leszczynski, S.R. Plimpton, P. Masłowski, A. Foltynowicz, J. Ye, B. McCollister, IEEE Trans. Plasma Sci. **40**, 8 (2012)
- S.R. Plimpton, M. Gólkowski, D.G. Mitchell, C. Austin, S.S. Eaton, G.R. Eaton, C. Gólkowski, M. Voskuil, Biotechnol. Bioeng. **110**, 7 (2013)
- P.J. Bruggeman, M.J. Kushner, B.R. Locke, J.G.E. Gardeniers, W.G. Graham, D.B. Graves, R.C.H.M. Hofman-Caris, D. Maric, J.P. Reid, E. Ceriani, D.F. Rivas, J.E. Foster, S.C. Garrick, Y. Gorbaney, S. Hamaguchi, F. Iza, H. Jablonowski, E. Klimova, J. Kolb, F. Krcma, P. Lukes, Z. Machala, I. Marinov, D. Mariotti, S.M. Thagard, D. Minakata, E.C. Neyts, J. Pawlat, Z.L. Petrovic, R. Pflieger, S. Reuter, D.C. Schram, S. Schröter, M. Shiraiwa, B. Tarabová, P.A. Tsai, J.R.R. Verlet, T.V. Woedtke, K.R. Wilson, K. Yasui, G. Zvereva, Plasma Sources Sci. Technol. **25**, 053002 (2016)
- H.Y. Kim, S.K. Kang, S.M. Park, H.Y. Jung, B.H. Choi, J.Y. Sim, J.K. Lee, Plasma Process. Polym. **12**, 1423 (2015)
- M. B. Cohen, US Patent, 10601125 B2 (2020)
- P.J. Singletary, M.B. Cohen, M.L.R. Walker, C.Y. Liu, C.Y. Chan, IEEE Trans. Plasma Sci. **48**, 1 (2020)
- C.Y. Liu, M.B. Cohen, M.L.R. Walker, IEEE Trans. Plasma Sci. **48**, 4 (2020)
- G.A. Mesyats, M.I. Yalandin, Physics-Uspekhi **48**, 3 (2005)
- Y. Fu, X. Wang, X. Zou, S. Yang, J.P. Verboncoeur, A.J. Christlieb, Phys. Plasmas **24**, 083510 (2017)
- T. Shao, G. Sun, P. Yan, S. Zhang, Jpn. J. Appl. Phys. **46**, 2 (2007)
- N.L. Bashlov, V.M. Milenin, G.J. Panasjuk, N.A. Timofeev, J. Phys. D **26**, 410 (1993)
- David B. Go, D.A. Pohlman, J. Appl. Phys. **107**, 103303 (2010)
- W. Zhang, T.S. Fisher, S.V. Garimella, J. Appl. Phys. **96**, 11 (2004)
- Z.L. Petrović, N. Škoro, D. Marić, C.M.O. Mahony, P.D. Maguire, M.R. Radenović, G. Malović, J. Phys. D Appl. Phys. **41**, 194002 (2008)
- M.R. Radjenović, J.K. Lee, Phys. Plasmas **12**, 063501 (2005)
- R. Massarczyk, P. Chu, C. Dugger, S.R. Elliott, K. Rielage, W. Xu, JINST **12**, P06019 (2017)
- M.U. Lee, J. Lee, J.K. Lee, G.S. Yun, Plasma Sources Sci. Technol. **28**, 034003 (2017)
- M. Puač, D. Marić, M.R. Radjenović, M. Šuvakov, Z.L. Petrović, Plasma Sources Sci. Technol. **27**, 075013 (2018)
- M.R. Radjenović, J.K. Lee, F. Iza, G.Y. Park, J. Phys. D Appl. Phys. **38**, 950 (2005)
- W.S. Boyle, P. Kisiuk, Phys. Rev. **97**, 2 (1955)
- D. Levko, L.L. Raja, Phys. Plasmas **22**, 123518 (2015)
- A. Bataller, J. Koulakis, S. Pree, S. Putterman, Appl. Phys. Lett. **105**, 223501 (2014)
- A.A. Kudryavtsev, A.I. Saifutdinov, M.S. Stefanova, P.M. Pramatarov, S.S. Sysoev, Phys. Plasmas **24**, 054507 (2017)
- L. Xu, A.V. Khrabrov, I.D. Kaganovich, T.J. Sommerer, Plasma Sources Sci. Technol. **27**, 104004 (2018)
- S.O. Macheret, M.N. Shneider, R.C. Murray, Phys. Plasmas **13**, 023502 (2006)
- S.O. Macheret, M.N. Shneider, Phys. Plasmas **20**, 101608 (2013)
- D. Levko, Ya. E. Krasik, J. Appl. Phys. **112**, 113302 (2012)
- D. Levko, S. Yatom, V. Vekselman, J.Z. Gleizer, V.T. Gurovich, Y.E. Krasik, J. Appl. Phys. **111**, 013304 (2012)
- Z. L. Petrović, S. Dujko, D. Marić, G. Malović, Ž. Nikitović, O. Šašić, J. Jovanović, V. Stojanović, M. R. Radenović, J. Phys. D Appl. Phys. **42**, 194002 (2009)
- Z.L. Petrović, D. Marić, M. Savić, S. Marjanović, S. Dujko, G. Malović, Plasma Process Polym. **14**, 1600124 (2017)
- H. Change, C.M. Ryu, S.J. Yoo, S.B. Kim, S.J. You, J. Phys. D Appl. Phys. **45**, 195206 (2012)
- J. Choi, F. Iza, J.K. Lee, C.M. Ryu, IEEE Trans. Plasma Sci. **35**, 5 (2007)
- H.C. Kim, J.K. Lee, Phys. Rev. Lett. **93**, 8 (2004)
- H.C. Kwon, S.Y. Jung, H.Y. Kim, I.H. Won, J.K. Lee, Phys. Plasmas **21**, 033511 (2014)
- H.C. Kwon, H.Y. Kim, I.H. Won, H.W. Lee, H.K. Shin, J.K. Lee, Phys. Plasmas **20**, 023506 (2013)
- F. Iza, J.K. Lee, M.G. Kong, Phys. Rev. Lett. **99**, 075004 (2007)
- J.P. Verboncoeur, M.V. Alves, V. Vahedi, C.K. Birdsall, J. Comput. Phys. **104**, 321 (1993)
- V. Vahedi, G. Dipeso, C.K. Birdsall, M.A. Lieberman, T.D. Rognlien, Plasma Sources Sci. Technol. **2**, 261 (1993)

45. H.C. Kim, F. Iza, S.S. Yang, M. Radmilović, J.K. Lee, J. Phys. D Appl. Phys. **38**, R283 (2005)
46. M.M. Turner, Phys. Plasmas **13**, 033506 (2006)
47. K.J. Chung, J.J. Dang, J.Y. Kim, W.H. Cho, Y.S. Hwang, New J. Phys. **18**, 105006 (2016)
48. M.A. Lieberman, A.J. Lichtenberg, *Principles of Plasma Discharges and Material Processing*, 2nd edn. (Wiley, New York, 2005), pp. 45, 691
49. U.S. Inan, M. Golkowski, *Principles of Plasma Physics for Engineers and Scientists, Chapter 7* (Wiley, New York, 2011)
50. J.T. Gudmundsson, A. Hecimovic, Plasma Sources Sci. Technol. **26**, 123001 (2017)
51. Y.P. Raizer, M.N. Shneider, High Temp. **27**, 329 (1989)
52. D. Levko, L.L. Raja, Phys. Plasmas **25**, 013509 (2018)
53. D. Levko, L.L. Raja, Phys. Plasmas **23**, 073513 (2016)
54. H.W. Lee, G.Y. Park, Y.S. Seo, Y.H. Im, S.B. Shim, H.J. Lee, J. Phys. D Appl. Phys. **44**, 053001 (2011)
55. Z. Donkó, S. Hamaguchi, T. Gans, Plasma Sources Sci. Technol. **27**, 054001 (2018)